Role of nematicity in controlling spin fluctuations and superconducting T_c in bulk FeSe

Swagata Acharya,[1,2,*] Dimitar Pashov,[2] and Mark van Schilfgaarde[2,3]
[1]*Institute for Molecules and Materials, Radboud University, NL-6525 AJ Nijmegen, The Netherlands*
[2]*King's College London, Theory and Simulation of Condensed Matter, The Strand, WC2R 2LS London, United Kingdom*
[3]*National Renewable Energy Laboratories, Golden, Colorado 80401, USA*

(Received 17 June 2021; revised 23 February 2022; accepted 14 April 2022; published 22 April 2022)

FeSe undergoes a transition from a tetragonal to a slightly orthorhombic phase at 90 K and becomes a superconductor below 8 K. The orthorhombic phase is sometimes called a nematic phase because quantum oscillation, neutron, and other measurements detect a significant asymmetry in x and y. How nematicity affects superconductivity has recently become a matter of intense speculation. Here, we employ an advanced *ab initio* Green's function description of superconductivity and show that bulk tetragonal FeSe would, in principle, superconduct with almost the same critical temperature T_c as the nematic phase. The mechanism driving the observed nematicity is not yet understood. Since the present theory underestimates it, we simulate the full nematic asymmetry by artificially enhancing the orthorhombic distortion. For benchmarking, we compare theoretical spin susceptibilities against experimentally observed data over all energies and relevant momenta. When the orthorhombic distortion is adjusted to correlate with observed nematicity in spin susceptibility, the enhanced nematicity causes spectral weight redistribution in the Fe-3d_{xz} and Fe-d_{yz} orbitals, but it leads to at most a 10–15% increment in T_c. This is because the d_{xy} orbital always remains the most strongly correlated and provides most of the source of the superconducting glue. Nematicity suppresses the density of states at the Fermi level; nevertheless, T_c increases, in contradiction to both BCS theory and the theory of Bose-Einstein condensation. We show how the increase is connected to the structure of the particle-particle vertex. Our results suggest that while nematicity may be an intrinsic property of bulk FeSe, it is not the primary force driving the superconducting pairing.

DOI: 10.1103/PhysRevB.105.144507

I. INTRODUCTION

Bulk FeSe superconducts up to 8 K, deep inside an orthorhombic phase that sets in at a much higher temperature, 90 K [1]. The normal bulk tetragonal phase does not superconduct unless it is doped [2–6] or forms a monolayer [7,8]. A nonalloy bulk tetragonal superconducting FeSe does not yet exist. This raises the question as to whether nematicity facilitates superconductivity in the bulk or not [9–11]. Further recent studies have suggested that spin fluctuations are strongly anisotropic, possibly originating from electronic nematicity inside the detwinned orthorhombic phase [12]. This enhanced electronic anisotropy shows up in the inelastic neutron scattering (INS), in resistivity measurements [13], in angle-resolved photoemission spectroscopic studies [14–16], and in several other measurements [17]. How such spin fluctuations affect the superconducting instability is a subject of intensive study.

Here, we take an *ab initio* Green's function approach to compare spin fluctuations and superconductivity in the orthorhombic phase with the tetragonal phase of bulk FeSe. This enables us to directly probe what role nematicity plays in governing these observed properties. To validate the theory, we perform rigorous benchmarking against existing susceptibility data from INS measurements [18]. Using the as-given orthorhombic structure, we show that spin susceptibilities are nearly indistinguishable for the two phases. To mimic the true nematicity, we enhance the small observed orthorhombic distortion by a factor of 5, to simulate the best possible agreement against the existing INS data inside the orthorhombic phase. While this enhanced structural nematicity has a different physical origin (most likely originating from a k-dependent vertex in the spin channel, or in the electron-phonon interaction), it provides a similar contribution to nematicity by adding an effective potential from a different source. As we show below, it enhances nematicity and generates a spin susceptibility that fairly well replicates nematicity observed in neutron measurements. We can then assess its impact on superconductivity, since spin fluctuations are the primary driving force for superconductivity, and we find that enhanced nematicity has only a very moderate effect.

II. METHODS

We believe that our findings are conclusive because they are obtained from a high-fidelity, *ab initio* description of spin fluctuations and superconductivity that depends only minimally on model assumptions. Our theory couples the (quasiparticle) self-consistent Hedin's *GW* approximation (QS*GW*) with dynamical mean-field theory (DMFT) [19–22]. Merging these two state-of-the-art methods captures the

*swagata.acharya@ru.nl

effect of both strong local dynamic spin fluctuations (captured well in DMFT) and nonlocal dynamic correlation [23,24] effects captured by QS*GW* [25]. On top of the DMFT self-energy, charge and spin susceptibilities are obtained from vertex functions computed from the two-particle Green's function generated in DMFT, via the solutions of the nonlocal Bethe-Salpeter equation (BSE). Additionally, we compute the particle-particle vertex functions and solve the ladder particle-particle BSE [21,26,27] to compute the superconducting susceptibilities and eigenvalues of superconducting gap instabilities.

Single-particle calculations [local-density approximation (LDA), and energy band calculations with the static quasiparticle QS*GW* self-energy $\Sigma^0(k)$] were performed on a $16 \times 16 \times 16\,k$ mesh, while the (relatively smooth) dynamical self-energy $\Sigma(k)$ was constructed using an $8 \times 8 \times 8\,k$ mesh and $\Sigma^0(k)$ was extracted from it. The same mesh is used for DMFT. We use QUESTAAL's all-electron implementation for all the calculations here; it was explained in detail in a recent methods paper [24]. For LDA we use a Barth-Hedin exchange-correlation functional. (QS*GW* does not depend on the LDA, but we nevertheless present LDA results to show how QS*GW* incorporates missing correlations from the LDA and renormalizes the electronic bands further.) The QS*GW* approximation, including the all-electron product basis used to make the polarizability and self-energy, is described in detail in Ref. [25]. Our one-particle basis set was constructed of 110 orbitals, including s, p, d, f, s, p, d orbitals centered on Fe augmented with local orbitals on the $4d$, and s, p, d, f, s, p, d orbitals centered on Se. The product basis in the augmentation spheres was expanded to $l = 8$ and included 520 orbitals; for the Coulomb interaction in the interstices a plane-wave cutoff of 2.3 Ry was used. The polarizability is computed with the tetrahedron method; for the self-energy a smearing of 0.003 Ry was used. For frequency integration, we used a mesh with 0.01 Ry spacing at low energy, gradually increasing at higher energy. Six points were used on the imaginary axis contribution to the self-energy. The charge density was made self-consistent though iteration in the QS*GW* self-consistency cycle: It was iterated until the root-mean-square change in Σ^0 reached 10^{-5} Ry. Thus the calculation was self-consistent in both $\Sigma^0(k)$ and the density. At the end of QS*GW* cycles, we use the quasiparticle electronic band structures as the starting point of our DMFT calculations. The impurity Hamiltonian is solved with the continuous-time quantum Monte Carlo (CTQMC) solver [28,29]. For projectors onto the Fe d subspace, we used projectors onto augmentation spheres, following the method described in Ref. [30]. DMFT is solved for all five Fe-$3d$ orbitals using CTQMC on a rotationally invariant Coulomb interaction. The double counting correlations are implemented using the fully localized limit approximation. The DMFT for the dynamical self-energy is iterated and converges in 30 iterations. Calculations for the single-particle response functions are performed with 10^9 quantum Monte Carlo (QMC) steps per core, and the statistics is averaged over 128 cores. The two-particle Green's functions are sampled over a larger number of cores (40 000–50 000) to improve the statistical error bars. The local effective interactions for the correlated impurity Hamiltonian are given by U and J. These are calculated within the constrained random-phase approximation (RPA) [31] from the QS*GW* Hamiltonian using an approach [21] similar to that of Ref. [32], but using projectors from Ref. [30]. For bulk FeSe we find $U = 3.5$ eV and $J = 0.6$ eV from our constrained RPA calculations. $\frac{J}{U} = 0.17$ suggests that the system is in the strong Hund's metallic limit as we have discussed in a prior work [33].

III. RESULTS

A. Computational details for magnetic susceptibility

We compute the local polarization bubble from the local single-particle Green's function computed from DMFT. We extract $\Gamma^{\rm irr}_{\rm loc}$, by solving the local Bethe-Salpeter equation which connects the local two-particle Green's function ($\chi_{\rm loc}$) sampled by CTQMC, with both the local polarization function ($\chi^0_{\rm loc}$) and $\Gamma^{\rm irr}_{\rm loc}$.

$$\Gamma^{{\rm irr},m(d)}_{{\rm loc}\,\alpha_3,\alpha_4}(i\nu, i\nu')_{i\omega} = \left[\left(\chi^0_{\rm loc}\right)^{-1}_{i\omega} - \chi^{m(d)-1}_{\rm loc}\right]_{\alpha_3,\alpha_4}(i\nu, i\nu')_{i\omega}. \quad (1)$$

Γ are the local irreducible two-particle vertex functions computed in magnetic (m) and density (d) channels. Γ is a function of two fermionic frequencies ν and ν' and the bosonic frequency ω.

Spin (χ^m) and charge (χ^d) susceptibilities are computed by solving the momentum-dependent Bethe-Salpeter equations in magnetic (spin) and density (charge) channels by dressing the nonlocal polarization bubble χ^0 with local irreducible vertex functions Γ in their respective channels:

$$\chi^{m(d)}_{\alpha_3,\alpha_4}(i\nu, i\nu')_{\mathbf{q},i\omega} = \left[(\chi^0)^{-1}_{\mathbf{q},i\omega} - \Gamma^{{\rm irr},m(d)}_{\rm loc}\right]^{-1}_{\alpha_3,\alpha_4}(i\nu, i\nu')_{\mathbf{q},i\omega}. \quad (2)$$

χ^0 is computed from single-particle DMFT Green's functions embedded in a QS*GW* bath. Susceptibilities $\chi^{m(d)}(\mathbf{q}, i\omega)$ are computed by summing over frequencies $(i\nu, i\nu')$ and orbitals $(\alpha_{1,2})$.

B. Benchmarking of magnetic susceptibilities against experimental observations

In Fig. 1 we plot the imaginary part of Im $\chi(q, \omega)$ along the $\mathbf{q} = (1, K)$ line of the one-atom Brillouin zone. Im $\chi(q, \omega)$ is computed in tetragonal and nematic phases and compared against the inelastic neutron scattering (INS) data received from Wang *et al.* [18]. Im$\chi(q, \omega)$ is plotted for slices $\omega =$ 15, 35, 40, and 80 meV. The ratio a/b in the orthorhombic phase ($a = 5.3100$ Å, $b = 5.3344$ Å) differs by only 0.4% from unity, and the area is only slightly smaller than the tetragonal phase ($a = 3.779$ Å, $\sqrt{2}a = 5.3443$ Å). Consequently, Im$\chi(q, \omega)$ changes little between tetragonal and orthorhombic phases. Most remarkably, the entire momentum dependence of Im$\chi(q, \omega)$ is rather well reproduced for the tetragonal phase at all energies. This is a testimony to the fact that the essential elements that are required to produce the momentum and energy structures for Im$\chi(q, \omega)$ are already present in the three-tier QS*GW*+DMFT+BSE approximation. Nevertheless, our computed Im$\chi(q, \omega)$ does not adequately reflect the effect of nematicity as is apparent in deviations of our theoretical data (red solid lines) from the experimental curves.

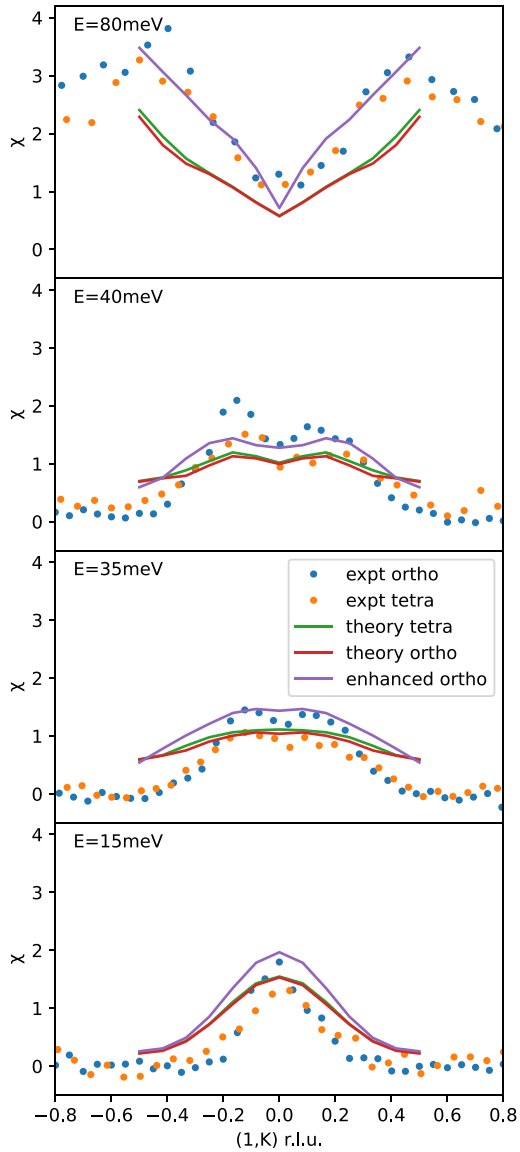

FIG. 1. Imaginary part of the dynamic spin susceptibility $\mathrm{Im}\chi(q,\omega)$ plotted along the line $\mathbf{q}=(H=1,K,L=0)$ in reciprocal lattice units (r.l.u.) of one Fe-atom unit cell. (H,K,L) is the standard notation used to identify reciprocal lattice directions. Experimentally, it is well established that the low-energy peak in $\mathrm{Im}\chi(q,\omega)$ is at $\mathbf{q}=(1,0,0)$ in the same notation. Different energy cuts were taken and plotted against the observed $\mathrm{Im}\chi(q,\omega)$ in an inelastic neutron scattering (INS) experiment by Wang *et al.* [18]. The experimental data are reproduced with the raw data received from Wang *et al.* We plot our computed $\mathrm{Im}\chi(q,\omega)$ at $\omega=15$, 35, 40, and 80 meV against the INS data. The theoretical data for the tetragonal (tetra; green solid line) and orthorhombic (ortho; red solid line) phases are nearly indistinguishable, and both sets of data deviate from the experimental data [the latter are plotted as orange (tetra) and blue (ortho) solid circles]. The theoretical data for the enhanced orthorhombic distortion (purple solid line) remarkably agree with the experimental INS data for all energy and momentum values.

These calculations show that nematicity probably originates from a momentum-dependent self-energy which contains a longer-range vertex beyond the single-site approximation in DMFT. Our DMFT spin vertex is local, and also we do not have the ability to include the electron-phonon interaction *ab initio*, one of which is likely to be responsible for the enhancement of the nematicity. We, instead, mimic the effective potential originating from either of these sources by modifying the crystal-field splitting, enlarging the orthorhombic splitting by a factor of 5 to ($a=5.3100$ Å, $b=5.4344$ Å). In the rest of this paper we use "ortho-enhanced" to identify this particular structure. We find that the resulting $\mathrm{Im}\chi(q,\omega)$ is enhanced in intensity and produces very good agreement with the INS data over all energy and momentum values.

The precise nature of the boson that is a Cooper pair in FeSe is debated, though generally the primary mechanism is believed to be magnetic fluctuations. This is supported by the observation of a negligible isotope effect in bulk FeSe [34]. Since the normal phase just above critical temperature $T_c=8$ K is orthorhombic, there has been much speculation that nematicity can be the mechanism driving superconductivity, though heavily debated. This is the question that we consider within the QSGW+DMFT theory. While it is conceivable that our fictitious inducement of nematicity does not yield the proper modification of superconductivity, the true mechanism would have to occur via some unknown process that does not involve the spin susceptibility (which we adequately reproduce, as we have shown). Thus we believe that modifying the effective potential via enhancing the orthorhombic distortion is a sufficient proxy to reliably pursue this question.

C. Effect of the nematic distortion of density of states

First, we study the effects of nematicity on the local density of states (DOS). The primary effect of nonlocal charge correlations included within QSGW is to reduce the bandwidth [see Figs. 2(a) and 2(b)] of FeSe compared with the LDA. We show results only for the orthorhombic phase of FeSe, but it is true irrespective of the structural phase considered. The effect of nematicity on d_{yz} and the effect of nematicity on d_{xz} are mirror images of each other [Figs. 2(d) and 2(e)]; this includes the change in DOS at E_F, $\rho(E_F)$. However, the enhanced orthorhombic distortion only weakly reduces the d_{xy} kinetic energy [Fig. 2(c)] and does not alter the xy contribution to $\rho(E_F)$. The Se-p states remain negligibly small within an energy range of ±1 eV around E_F in all cases. In Fig. 2(b) the Se-p DOS is shown scaled by a factor of 10 to make it visible. The effect of such distortions is negligible on the Se-p states as well, and these states remain irrelevant for the low-energy physics of FeSe.

Figure 2(f) plots the QSGW+DMFT DOS for the three systems: tetragonal, orthorhombic, and ortho-enhanced. Note that the QSGW Green's functions are renormalized in the presence of the self-consistent single-site DMFT self-energy. For all phases there is a significant drop in $\rho(E)$ at $\omega=0$, and it is also seen that enhanced nematicity modestly suppresses $\rho(E_F)$ (i.e., $\omega=0$). This observation suggests that photoemission spectroscopy should be able to see this drop in the local DOS at low energies in systems where nematicity plays a major role, for example, in the detwinned sample of FeSe [12,15,35]. It suggests that if the superconductivity is modified by enhanced nematicity, it does not result from a purely Fermi surface nesting driven mechanism. Within a purely BCS picture such a dip in $\rho(E_F)$ would produce

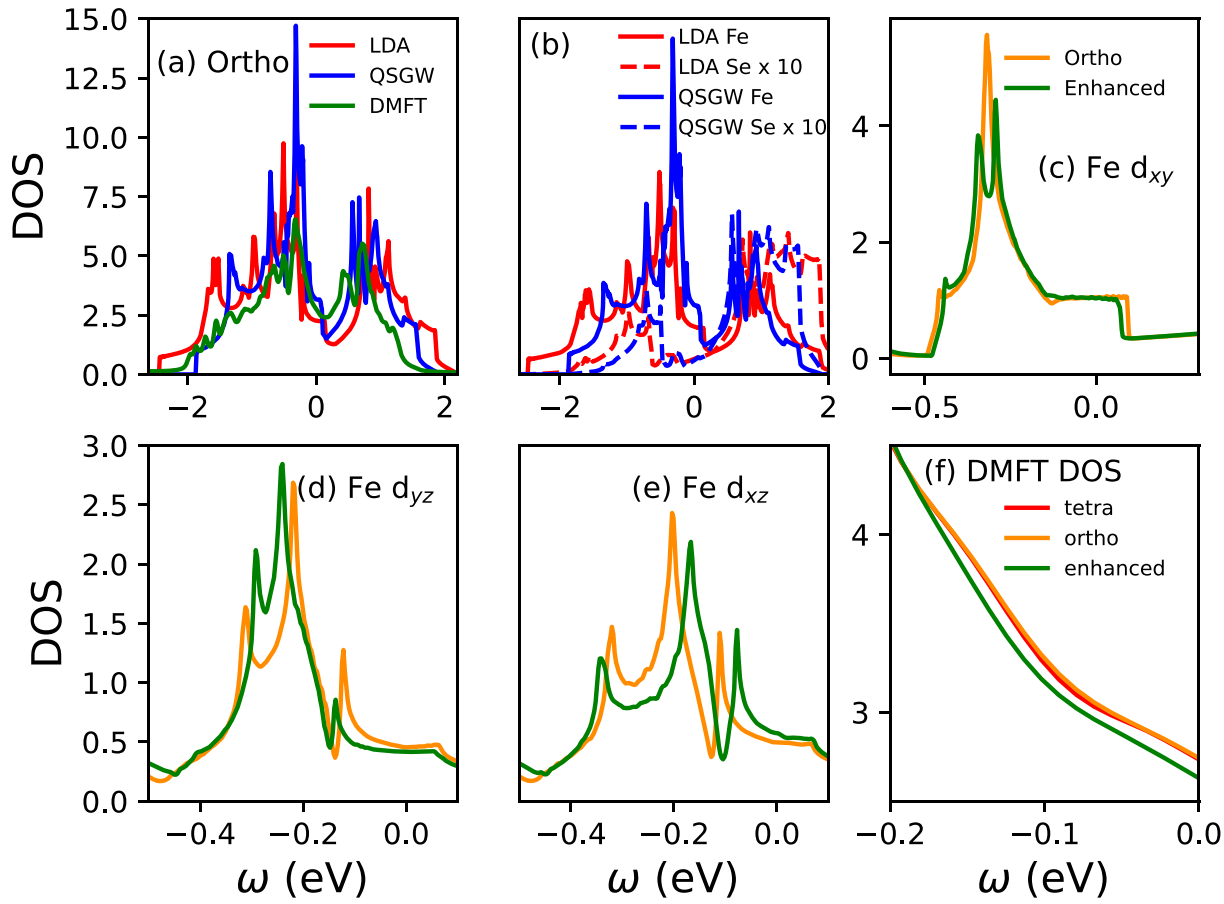

FIG. 2. (a) The QSGW total local density of states (DOS) for FeSe is narrower compared with the LDA. DMFT narrows the bands compared with QSGW. (b) Both Fe-3d states and Se-p states get narrowed within QSGW, although the Se-p states are negligibly small around E_F. (c)–(f) The artificially enhanced nematic distortion reduces the Fe-d_{xy} bandwidth weakly compared with the original nematic phase (c); however, its effects on d_{yz} (d) and d_{xz} (e) orbitals are opposite: In one case, the DOS at E_F drops, and in the other case it is enhanced. (f) The total QSGW+DMFT local density of states (DOS) for FeSe in the tetragonal, orthorhombic, and orthorhombic phase with enhanced distortion is shown.

exponentially weak suppression of superconducting T_c. Even while nematicity reduces $\rho(E_F)$, it has the opposite effect on T_c. As we will show in the following discussion, T_c increases as a consequence of the change in the two-particle vertex which promotes the superconducting pairing glue.

D. Orbitally resolved magnetic susceptibilities

Before moving on to the discussion of superconductivity, we analyze our computed spin susceptibilities $\chi(q,\omega)$, particularly in an attempt to understand its orbital structure. We show in Fig. 3(a) that the irreducible vertex computed using CTQMC+DMFT is strongly orbital dependent. It is crucially important that CTQMC+DMFT is site-local but not point-local. One of the primary successes of DMFT is its ability to pick up orbital-dependent structures in self-energy and higher-order vertex functions. This becomes even more crucial in Hund's metals since Hund's J generates strong orbital differentiation. The local irreducible vertex computed in the magnetic channel depends on three frequencies (two Matsubara fermionic frequency indices $\omega_{1,2}$ and one Matsubara bosonic frequency index Ω). We show that for all energies (Matsubara fermionic frequencies) the magnetic vertex Γ remains larger in the d_{xy} channel compared with the $d_{xz,yz}$ channels, suggesting that magnetic scatterings are largest there.

The site-local vertex has a pronounced effect on the both the magnitude and momentum dependence of the nonlocal χ [compare RPA with BSE in Fig. 3(b)], and it is the vertex that ensures that the antiferromagnetic instability suppresses magnetic instabilities at other q. χ^{RPA} must be scaled by 8 or so to put on the same scale as χ^{BSE}, which gives a rough measure of the Stoner enhancement. However, it is important to stress once again that the orbital and frequency dependence of the vertex is crucial, and it cannot be adequately modeled by a constant.

We resolve the computed static spin susceptibilities $\chi(q)$ in different intraorbital channels. Enhanced nematicity causes $\chi(q)$ to increase in all intraorbital channels; however, it remains smaller in the d_{xz} and d_{yz} channels than in the d_{xy} channel [see Figs. 3(c)–3(f)]. Orthorhombic distortion lifts the degeneracy between the d_{xz} and d_{yz} orbitals that is observed in neutron measurements. In any case, the d_{xy} channel remains the dominant spin fluctuation channel, while the d_{xz} and d_{yz} channels each contribute nearly 40% of the d_{xy} spin fluctuations. This is crucial. Although this desired "nematic"

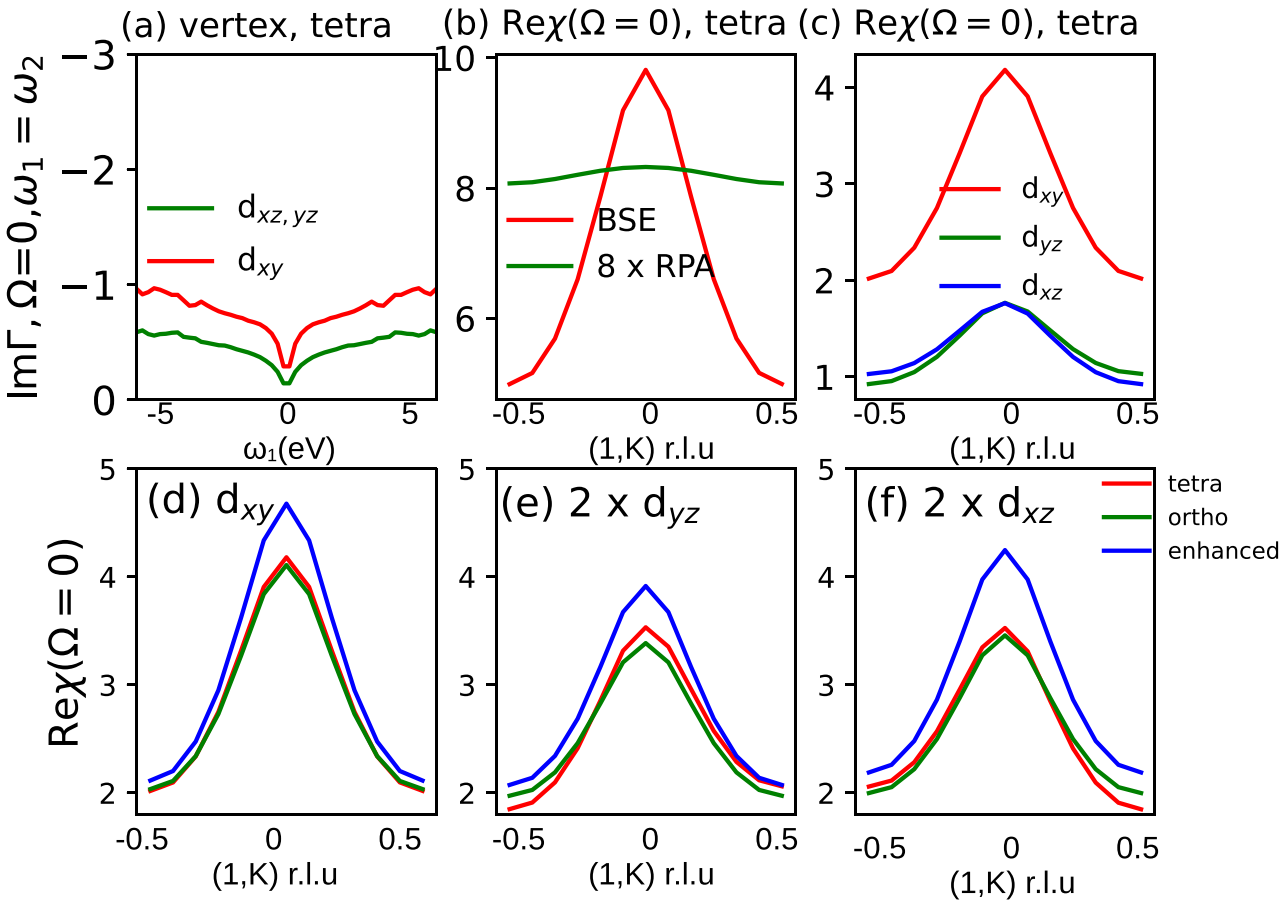

FIG. 3. (a) The magnetic vertex and its orbital structure. For all energies, $\Gamma_{xy} > \Gamma_{xz,yz}$. (b) The BSE approximation is shown to strongly modify the random-phase approximation (RPA) in the magnetic channel, in a momentum-dependent way (note that χ^{RPA} is scaled by a factor of 8). (c)–(f) Orbitally resolved static spin susceptibility, $\text{Re}\chi(q)$, is plotted along $\mathbf{q} = (H, K, L = 0)$. The enhanced orthorhombic distortion increases the intensity of $\text{Re}\chi(q)$ in all intraorbital channels; however, the d_{xy} states remain dominant in all cases. χ_{xz} and χ_{yz} are scaled by a factor of 2 to improve visibility.

distortion, which produces the agreement with experimentally observed $\chi(q, \omega)$, leads to moderate spectral weight redistribution between the d_{xz} and d_{yz} one-particle channels, d_{xy} still remains the most correlated orbital that hosts the largest fraction of the magnetic collective fluctuations in the system.

E. Computational details of superconducting instabilities

How particular orbitals govern spin fluctuations and thus control T_c is key to understanding the superconducting mechanism in such a complex multiband manifold. We probe the effect of such enhanced nematicity on the superconductivity. The superconducting pairing susceptibility $\chi^{\text{p-p}}$ is computed by dressing the nonlocal pairing polarization bubble $\chi^{0,\text{p-p}}(\mathbf{k}, i\nu)$ with the pairing vertex $\Gamma^{\text{irr,p-p}}$ using the Bethe-Salpeter equation in the particle-particle (p-p) channel.

$$\chi^{\text{p-p}} = \chi^{0,\text{p-p}} \cdot [\mathbf{1} + \Gamma^{\text{irr,p-p}} \cdot \chi^{0,\text{p-p}}]^{-1}. \tag{3}$$

The particle-particle vertex in the singlet channel has odd symmetry under the exchange of two external spins,

$$\Gamma^{\text{p-p},s} = \tfrac{1}{2}\Big[\Gamma^{\text{p-p}}_{\substack{\uparrow\downarrow \\ \downarrow\uparrow}} - \Gamma^{\text{p-p}}_{\substack{\uparrow\uparrow \\ \downarrow\downarrow}}\Big]. \tag{4}$$

The irreducible particle-particle vertex function channel $\Gamma^{\text{p-p,irr}}$, which provides the pairing glue to form Cooper pairs, consists of the fully irreducible vertex function $\Gamma^{f,\text{irr}}$ and the reducible vertex functions computed in the particle-hole (p-h) channels

$$\widetilde{\Gamma}^{\text{p-h}} = \Gamma^{\text{full,p-h}} - \Gamma^{\text{irr,p-h}}, \tag{5}$$

where

$$\Gamma^{\text{full}} = \Gamma^{\text{irr}} - \Gamma^{\text{irr}}\chi\Gamma^{\text{irr}}. \tag{6}$$

This results in

$$\widetilde{\Gamma}^{\text{p-h}} = \Gamma^{\text{irr}}\chi\Gamma^{\text{irr}}. \tag{7}$$

This is one of the most crucial points of our implementation. Note that the $\Gamma^{f,\text{irr}}$ is local within the single-site DMFT approximation and hence cannot contribute to superconductivity. Nevertheless, the reducible magnetic or charge vertex $\widetilde{\Gamma}^{\text{irr,p-h}}$, obtained from dressing Γ^{irr} with the full nonlocal and dynamic magnetic or charge susceptibilities, can have both momentum dependence and dynamics desired for superconductivity. The parquetlike equations that are solved to achieve

this are as follows:

$$\widetilde{\Gamma}^{\text{p-h},m/d}_{\substack{\alpha_2,\alpha_4\\ \alpha_1,\alpha_3}}(i\nu', i\nu)_{\mathbf{q},i\omega} = \sum_{i\nu 1, i\nu 2} \sum_{\substack{\alpha_2',\alpha_4'\\ \alpha_3',\alpha_1'}} \Gamma^{\text{irr,p-h},m/d}_{\text{loc}\ \substack{\alpha_2,\alpha_2'\\ \alpha_1,\alpha_1'}}(i\nu, i\nu 1)_{i\omega} \cdot \chi^{\text{p-h},m/d}_{\mathbf{q}\ \substack{\alpha_2',\alpha_4'\\ \alpha_1',\alpha_3'}}(i\nu 1, i\nu 2)_{i\omega} \cdot \Gamma^{\text{irr,p-h},m/d}_{\text{loc}\ \substack{\alpha_4',\alpha_4\\ \alpha_3',\alpha_3}}(i\nu 2, i\nu')_{i\omega}. \quad (8)$$

The irreducible particle-particle vertex function $\Gamma^{\text{irr,p-p}}$ is finally written in terms of the reducible magnetic or charge vertex $\widetilde{\Gamma}^{m/d}$ functions.

$$\Gamma^{\text{irr,p-p}}_{\substack{\alpha_2\uparrow,\alpha_4\downarrow\\ \alpha_1\uparrow,\alpha_3\downarrow}}(\mathbf{k}, i\nu, \mathbf{k}', i\nu') = \Gamma^{f,\text{irr}}_{\substack{\alpha_2\uparrow,\alpha_4\downarrow\\ \alpha_1\uparrow,\alpha_3\downarrow}}(i\nu, i\nu') - \tfrac{1}{2}[\widetilde{\Gamma}^{\text{p-h},(d)} - \widetilde{\Gamma}^{\text{p-h},(m)}]_{\substack{\alpha_2,\alpha_3\\ \alpha_1,\alpha_4}}(\mathbf{k}' - \mathbf{k}, i\nu' - i\nu) + \widetilde{\Gamma}^{\text{p-h},(m)}_{\substack{\alpha_4,\alpha_3\\ \alpha_1,\alpha_2}}(-\mathbf{k}' - \mathbf{k}, -i\nu' - i\nu), \quad (9)$$

$$\Gamma^{\text{irr,p-p}}_{\substack{\alpha_2\downarrow,\alpha_4\uparrow\\ \alpha_1\uparrow,\alpha_3\downarrow}}(\mathbf{k}, i\nu, \mathbf{k}', i\nu') = \Gamma^{f,\text{irr}}_{\substack{\alpha_2\downarrow,\alpha_4\uparrow\\ \alpha_1\downarrow,\alpha_3\uparrow}}(i\nu, i\nu') - \tfrac{1}{2}[\widetilde{\Gamma}^{\text{p-h},(d)} - \widetilde{\Gamma}^{\text{p-h},(m)}]_{\substack{\alpha_4,\alpha_3\\ \alpha_1,\alpha_2}}(-\mathbf{k}' - \mathbf{k}, -i\nu' - i\nu) - \widetilde{\Gamma}^{\text{p-h},(m)}_{\substack{\alpha_2,\alpha_3\\ \alpha_1,\alpha_4}}(\mathbf{k}' - \mathbf{k}, i\nu' - i\nu). \quad (10)$$

Finally, exploiting Eqs. (6) and (7) and Eqs. (9) and (10), we obtain the $\Gamma^{\text{irr,p-p}}$ in the singlet channel from the magnetic and density particle-hole reducible vertices,

$$\Gamma^{\text{irr,p-p},s}_{\substack{\alpha_2,\alpha_4\\ \alpha_1,\alpha_3}}(\mathbf{k}, i\nu, \mathbf{k}', i\nu') = \Gamma^{f,\text{irr}}_{\substack{\alpha_2,\alpha_4\\ \alpha_1,\alpha_3}}(i\nu, i\nu') + \tfrac{1}{2}\big[\tfrac{3}{2}\widetilde{\Gamma}^{\text{p-h},(m)} - \tfrac{1}{2}\widetilde{\Gamma}^{\text{p-h},(d)}\big]_{\substack{\alpha_2,\alpha_3\\ \alpha_1,\alpha_4}}(i\nu, -i\nu')_{\mathbf{k}'-\mathbf{k}, i\nu'-i\nu} + \tfrac{1}{2}\big[\tfrac{3}{2}\widetilde{\Gamma}^{\text{p-h},(m)} - \tfrac{1}{2}\widetilde{\Gamma}^{\text{p-h},(d)}\big]_{\substack{\alpha_4,\alpha_3\\ \alpha_1,\alpha_2}}(i\nu, i\nu')_{-\mathbf{k}'-\mathbf{k}, -i\nu'-i\nu}. \quad (11)$$

With $\Gamma^{\text{irr,p-p}}$ in hand we can solve the p-p BSE to compute the p-p susceptibility $\chi^{\text{p-p}}$.

$$\chi^{\text{p-p}} = \chi^{0,\text{p-p}} \cdot [\mathbf{1} + \Gamma^{\text{irr,p-p}} \cdot \chi^{0,\text{p-p}}]^{-1}. \quad (12)$$

The critical temperature T_c is determined by the temperature where $\chi^{\text{p-p}}$ diverges. For such divergence the sufficient condition is that at least one eigenvalue of the pairing matrix $-\Gamma^{\text{irr,p-p}} \cdot \chi^{0,\text{p-p}}$ approaches unity. The corresponding eigenfunction represents the momentum structure of $\chi^{\text{p-p}}$. Hence T_c, eigenvalues λ, and eigenfunctions ϕ^{λ} associated with different superconducting gap symmetries (in the singlet channel) can all be computed by solving the eigenvalue equation,

$$\frac{T}{N_k}\sum_{k',i\nu'}\sum_{\substack{\alpha_2\alpha_4\\ \alpha_5,\alpha_6}} \Gamma^{\text{irr,p-p},s}_{\substack{\alpha_2,\alpha_4\\ \alpha_1,\alpha_3}}(k, i\nu, k', i\nu') \cdot \chi^{0,\text{p-p}}_{\substack{\alpha_5,\alpha_6\\ \alpha_2,\alpha_4}}(k, i\nu')\phi^{\lambda}_{\alpha_5\alpha_6} = \lambda \cdot \phi^{\lambda}_{\alpha_5\alpha_6}. \quad (13)$$

The gap function can be written in a symmetric and Hermitian form by

$$\frac{T}{N_k}\sum_{k',i\nu'}\sum_{\substack{\alpha_2\alpha_4\alpha_5\\ \alpha_6\alpha_7\alpha_8}} \Big(\chi^{0,\text{p-p}}_{\substack{\alpha_2,\alpha_4\\ \alpha_1,\alpha_3}}(k, i\nu)\Big)^{1/2} \times \Gamma^{\text{irr,p-p},s}_{\substack{\alpha_5,\alpha_7\\ \alpha_2,\alpha_4}}(k, i\nu, k', i\nu') \cdot \Big(\chi^{0,\text{p-p}}_{\substack{\alpha_6,\alpha_8\\ \alpha_5,\alpha_7}}(k', i\nu')\Big)^{1/2} \times \phi^{\lambda}_{\alpha_6\alpha_8}(k', i\nu') = \lambda \cdot \phi^{\lambda}_{\alpha_1\alpha_3}(k, i\nu). \quad (14)$$

It can be explicitly shown that the eigenvalues of the non-Hermitian gap equation are the same as eigenvalues of the Hermitian gap equation.

Finally, $\chi^{\text{p-p}}$ can be represented in terms of eigenvalues λ and eigenfunctions ϕ^{λ} of the Hermitian particle-particle pairing matrix.

$$\chi^{\text{p-p}}(k, i\nu, k', i\nu') = \sum_{\lambda} \frac{1}{1-\lambda} \cdot (\sqrt{\chi^{0,\text{p-p}}(k, i\nu)} \cdot \phi^{\lambda}(k, i\nu)) \times (\sqrt{\chi^{0,\text{p-p}}(k', i\nu')} \cdot \phi^{\lambda}(k', i\nu')). \quad (15)$$

To solve this eigenvalue equation, the most important approximation we make is to take the static limit of $\Gamma^{\text{irr,p-p}}$ in the bosonic frequency $i\omega = 0$ (real frequency axis). The explicit dependence on the fermion frequencies is kept, as are all the orbital and momentum indices.

As is apparent from Eq. (11), at what wave vector spin and charge fluctuations are strong is of central importance to the kind of superconducting pairing symmetry they can form. The entire momentum, orbital, and frequency dependences of the vertex functions are computed explicitly, and the BSE equations are solved with them. Since the vertex structure has no predefined form factor, the emergent superconducting gap symmetry is calculated in an unbiased manner. This provides an unbiased insight into the superconducting gap symmetries and the strength of the leading eigenvalues in different systems and, most importantly, allows for a fair comparison of the relative strength of the leading superconducting instabilities in bulk tetragonal, orthorhombic, and ortho-enhanced FeSe. Thus our ability to predict these properties is limited mostly by the fidelity of the Green's functions that determine the vertices and χ. Furthermore, the fact that the charge component to the superconducting vertex is finite, within our formulation, ensures that the magnetic (in this case, antiferromagnetic) instability cannot drive an order and suppress superconductivity, as naturally happens with density functional and other mean-field approaches. We show in Fig. 4(a) that the antiferromagnetic instability remains the subleading instability in FeSe making way for superconductivity to take place.

There is a practical limitation, however, since we compute the vertex functions from CTQMC, which limits the temperatures down to which the vertex can be computed. We have observed in different materials that the leading eigenvalue λ does not have a simple, analytic dependence on temperature [36], and hence λ cannot be reliably extrapolated to very low temperatures. For that reason, we avoid estimating T_c (the temperature at which λ reaches 1) for different systems from our method; rather, we compare the strength of λ for a given temperature in different materials (Fig. 4), which is free

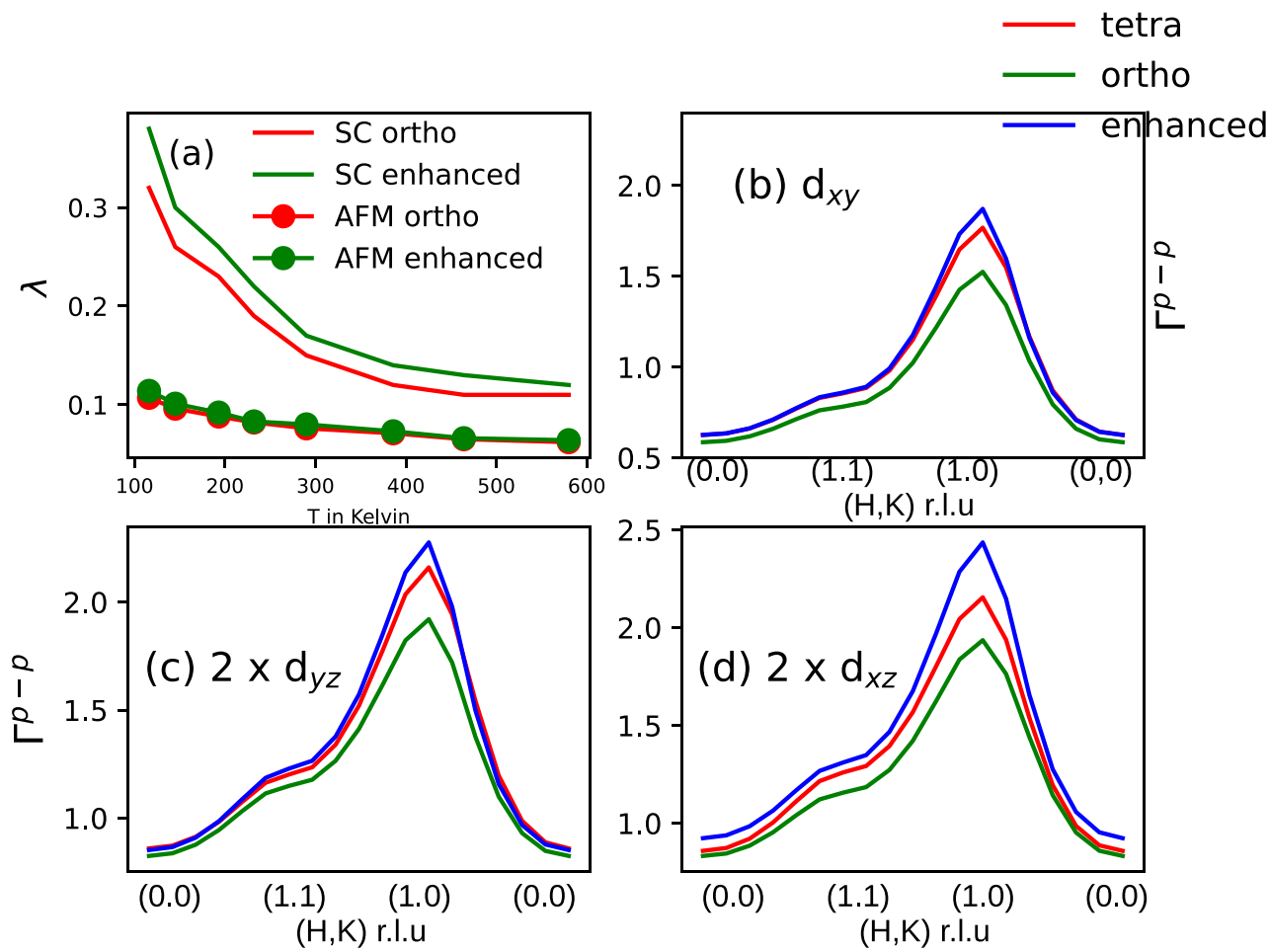

FIG. 4. (a) The leading instability in the superconducting channel is shown to dominate over the magnetic instability for all temperatures. In (b)–(d) the momentum structure of the particle-particle vertex is shown. The particle-particle instability remains at least twice larger in the d_{xy} channel in all phases of FeSe compared with the d_{yz} and d_{xz} channels.

from any ambiguities. We have explored the fidelity of this implementation in predicting the gap symmetries and leading instabilities in several previous works [33,36,37].

F. Leading and subleading superconducting instabilities

We observe that the leading eigenvalue λ (Fig. 4) of the superconducting gap equation corresponds to an extended *s*-wave gap structure [38], with a form factor $\Delta_1 \sim \cos(k_x) + \cos(k_y)$ (see Fig. 5) in all the phases. The lagging instability Δ_2 has a $\cos(k_x) - \cos(k_y)$ structure. Moreover, this dominant instability exists in the d_{xy} orbital channel (Fig. 4) consistent with our observations of dominant spin fluctuations in the same channel. To see what controls the instability, it is simplest to consider what increases $\Gamma^{\text{p-p}} \cdot \chi^0$; see Eq. (12). We find that the orthorhombic distortion weakly affects both χ^0 [seen from the change in DOS; Fig. 2(f)] and $\Gamma^{\text{p-p}}$ (Fig. 4) relative to the tetragonal phase, and hence $\Gamma^{\text{p-p}} \cdot \chi^0$ hardly changes. However, in the ortho-enhanced case, $\Gamma^{\text{p-p}}$ increases while χ^0 drops. The increment in $\Gamma^{\text{p-p}}$ overcompensates the reduction in χ^0, so that $\Gamma^{\text{p-p}} \cdot \chi^0$ is enhanced relative to the tetragonal phase. We stress that the modest enhancement to T_c occurs for reasons completely different from approaches to superconductivity that rely on the BCS approximation or its extension. Within BCS any changes to the superconducting T_c are primarily discussed with arguments based on density of states. This is natural since the replacement of the density ρ by $\rho(E_F)$ in BCS gap integrals is strictly possible only within the BCS approximation $E_F \gg \hbar\omega_D \gg \Delta_0$ (where ω_D is the phonon frequency and Δ_0 is the superconducting gap at $T = 0$). Based on BCS theory [39], a small suppression in $\rho(\text{E}_F)$ would cause an exponentially small reduction in T_c. Furthermore, in the limit of strong electron-electron interaction (attraction) for dilute mobile charges, T_c is given by the Bose-Einstein condensation (BEC) temperature [40–42], and not by the BCS limit. In BEC, T_c has a power-law dependence on ρ in contrast to the exponential dependence in BCS. The famous Uemura plot [43], as was established in the early days of cuprates, showed how unconventional superconductivity in cuprates was more akin to the BEC limit, instead of the BCS limit. Nevertheless, in FeSe the BEC formula would again lead to weak suppression of T_c due to nematicity. In stark contrast, within our implementation of this finite-temperature instability approach to superconductivity, no such approximations are made; moreover, we keep the full energy dynamics of the one-particle Green's functions and full energy dynamics (dependence on two Matsubara fermionic frequency indices and one Matsubara bosonic frequency index) of the

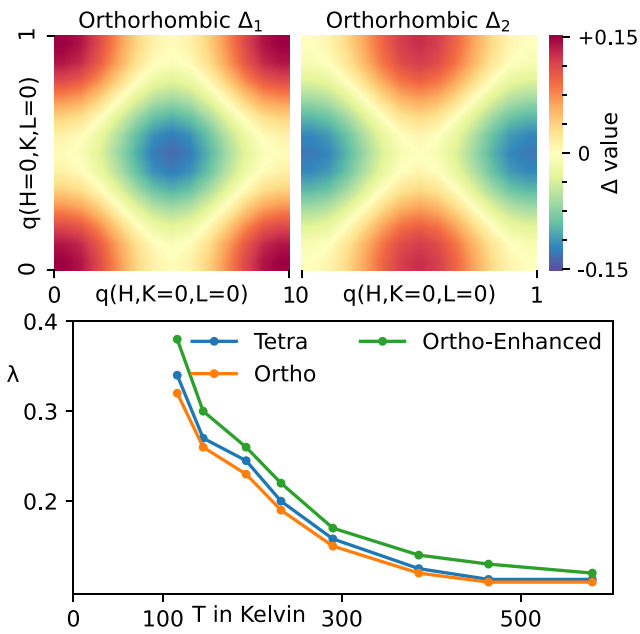

FIG. 5. The superconducting instabilities inside the orthorhombic phase are shown: Instabilities correspond to the leading (Δ_1) and and lagging (Δ_2) eigenvalues of the solutions to the BCS gap equation. The evolution of the leading eigenvalue as a function of temperature is shown for tetragonal, orthorhombic, and ortho-enhanced phases in the bottom panel.

two-particle vertex functions $\Gamma^{\text{p-p}}$. The approximation we do make, namely, setting the bosonic frequency to zero while diagonalizing the gap equation, is a sensible one that assumes that superconductivity is a low-energy phenomenon. As noted, the full theory also predicts that nematicity slightly enhances T_c, because of changes to the vertex.

As we showed in our recent work [36], it is extremely challenging to perform the calculations at a low enough temperature where λ can reach unity, owing to several technicalities primarily related to the stochastic nature of the CTQMC solver. The lowest temperature at which we could perform our calculations in these systems is 116 K, where λ remains less than unity. However, following the trend, it appears that the ortho-enhanced phase can at most realize a 10–15% enhancement in T_c in comparison to the bulk orthorhombic phase. Our calculations suggest that the tetragonal phase could also superconduct with a T_c not much different from the ortho-enhanced phase. This is consistent with the experimental observation that the $FeSe_{1-x}S_x$ alloy realizes a superconducting T_c not significantly different from the bulk orthorhombic FeSe, even when sulfur doping suppresses the nematic phase completely [44–46]. The primary origin of this, as we show, is that in bulk FeSe, in all the phases, the Fe-$3d_{xy}$ orbital remains the most correlated orbital that sources the largest fraction of collective magnetic fluctuations and thus acts as the primary glue for the Cooper pair formation. However, as we explicitly show in Figs. 4(b)–4(d), it is not only the magnetic susceptibilities but also the particle-particle vertex $\Gamma^{\text{p-p}}$, which is a complicated combination of both magnetic and charge vertex functions [see Eq. (11)], that remain most dominant in the d_{xy} channel in all phases of bulk FeSe. While nematic distortions drive spectral weight redistribution mediated by degeneracy lifting of d_{xz} and d_{yz} orbitals, they act as subleading channels for magnetism and superconductivity.

IV. CONCLUSIONS

To summarize, we perform *ab initio* calculations for bulk tetragonal and orthorhombic phases of FeSe and compute single- and two-particle spectra and superconducting eigenvalues. We find that spin fluctuations are dominant in the Fe-$3d_{xy}$ channel in all cases and can potentially drive superconductivity in the bulk tetragonal FeSe. Nevertheless, a rigorous comparison against the observed spin susceptibilities in inelastic neutron scattering experiments in the orthorhombic phase reveals that our computed susceptibilities have the correct momentum structure at all energies, but not the intensity. We show that an artificially enhanced structural orthorhombic distortion simulates the missing spin fluctuation intensity and acts as the proxy for the desired nematicity, missing from our theory but present in the real world. This enhanced nematicity, even while suppressing the one-particle density of states at the Fermi energy, nevertheless leads to enhanced correlations from the particle-particle superconducting correlations, leading to an increment in T_c on the order of 10–15%.

ACKNOWLEDGMENTS

We thank Qisi Wang and Jun Zhao for sharing with us the raw data for spin susceptibilities. This work was supported by the Simons Collaboration on the Many-Electron Problem. S.A. was supported (in later stages of this work) by the ERC Synergy Grant, Project No. 854843 FASTCORR (Ultrafast Dynamics of Correlated Electrons in Solids). M.v.S. and D.P. were supported by the U.S. Department of Energy, Office of Science, Basic Energy Sciences, under Award No. FWP ERW7906. We acknowledge PRACE for awarding us access to SuperMUC at the GCS at LRZ, Germany; Irene-Rome hosted by TGCC, France; the STFC Scientific Computing Department's SCARF cluster; and the Cambridge Tier-2 system operated by the University of Cambridge Research Computing Service [47] funded by EPSRC Tier-2 Capital Grant No. EP/P020259/1. This work was also partly carried out on the Dutch National e-Infrastructure with the support of the SURF Cooperative.

[1] T. M. McQueen, A. J. Williams, P. W. Stephens, J. Tao, Y. Zhu, V. Ksenofontov, F. Casper, C. Felser, and R. J. Cava, Phys. Rev. Lett. **103**, 057002 (2009).

[2] Y. Mizuguchi, F. Tomioka, S. Tsuda, T. Yamaguchi, and Y. Takano, Appl. Phys. Lett. **93**, 152505 (2008).

[3] R. Shipra, H. Takeya, K. Hirata, and A. Sundaresan, Physica C (Amsterdam) **470**, 528 (2010).

[4] A. Galluzzi, M. Polichetti, K. Buchkov, E. Nazarova, D. Mancusi, and S. Pace, Supercond. Sci. Technol. **30**, 025013 (2016).

[5] F. Sun, Z. Guo, H. Zhang, and W. Yuan, J. Alloys Compd. **700**, 43 (2017).

[6] L. Craco, M. Laad, and S. Leoni, in *VII Brazilian Meeting on Simulational Physics 510 August 2013, Joao Pessoa, Paraiba, Brazil*, Journal of Physics: Conference Series Vol. 487 (Institute of Physics, Bristol, 2014), p. 012017.

[7] Q.-Y. Wang, Z. Li, W.-H. Zhang, Z.-C. Zhang, J.-S. Zhang, W. Li, H. Ding, Y.-B. Ou, P. Deng, K. Chang, J. Wen, C.-L. Song, K. He, J.-F. Jia, S.-H. Ji, Y.-Y. Wang, L.-L. Wang, X. Chen, X.-C. Ma, and Q.-K. Xue, Chin. Phys. Lett. **29**, 037402 (2012).

[8] J.-F. Ge, Z.-L. Liu, C. Liu, C.-L. Gao, D. Qian, Q.-K. Xue, Y. Liu, and J.-F. Jia, Nat. Mater. **14**, 285 (2015).

[9] A. E. Böhmer and A. Kreisel, J. Phys.: Condens. Matter **30**, 023001 (2017).

[10] A. V. Chubukov, M. Khodas, and R. M. Fernandes, Phys. Rev. X **6**, 041045 (2016).

[11] Q. Wang, Y. Shen, B. Pan, Y. Hao, M. Ma, F. Zhou, P. Steffens, K. Schmalzl, T. Forrest, M. Abdel-Hafiez, X. Chen, D. A. Chareev, A. N. Vasiliev, P. Bourges, Y. Sidis, H. Cao, and J. Zhao, Nat. Mater. **15**, 159 (2016).

[12] T. Chen, Y. Chen, A. Kreisel, X. Lu, A. Schneidewind, Y. Qiu, J. Park, T. G. Perring, J. R. Stewart, H. Cao, R. Zhang, Y. Li, Y. Rong, Y. Wei, B. M. Andersen, P. J. Hirschfeld, C. Broholm, and P. Dai, Nat. Mater. **18**, 709 (2019).

[13] M. A. Tanatar, A. E. Böhmer, E. I. Timmons, M. Schütt, G. Drachuck, V. Taufour, K. Kothapalli, A. Kreyssig, S. L. Bud'ko, P. C. Canfield, R. M. Fernandes, and R. Prozorov, Phys. Rev. Lett. **117**, 127001 (2016).

[14] M. D. Watson, T. K. Kim, L. C. Rhodes, M. Eschrig, M. Hoesch, A. A. Haghighirad, and A. I. Coldea, Phys. Rev. B **94**, 201107(R) (2016).

[15] M. D. Watson, A. A. Haghighirad, L. C. Rhodes, M. Hoesch, and T. K. Kim, New J. Phys. **19**, 103021 (2017).

[16] A. I. Coldea and M. D. Watson, Annu. Rev. Condens. Matter Phys. **9**, 125 (2018).

[17] A. Böhmer, T. Arai, F. Hardy, T. Hattori, T. Iye, T. Wolf, H. V. Löhneysen, K. Ishida, and C. Meingast, Phys. Rev. Lett. **114**, 027001 (2015).

[18] Q. Wang, Y. Shen, B. Pan, X. Zhang, K. Ikeuchi, K. Iida, A. Christianson, H. C. Walker, D. T. Adroja, M. Abdel Hafiez, X. Chen, D. A. Chareev, A. N. Vasiliev, and J. Zhao, Nat. Commun. **7**, 12182 (2016).

[19] L. Sponza, P. Pisanti, A. Vishina, D. Pashov, C. Weber, M. van Schilfgaarde, S. Acharya, J. Vidal, and G. Kotliar, Phys. Rev. B **95**, 041112(R) (2017).

[20] S. Acharya, D. Dey, T. Maitra, and A. Taraphder, J. Phys. Commun. **2**, 075004 (2018).

[21] S. Acharya, D. Pashov, C. Weber, H. Park, L. Sponza, and M. Van Schilfgaarde, Commun. Phys. **2**, 163 (2019).

[22] E. Baldini, M. A. Sentef, S. Acharya, T. Brumme, E. Sheveleva, F. Lyzwa, E. Pomjakushina, C. Bernhard, M. van Schilfgaarde, F. Carbone, A. Rubio, and C. Weber, Proc. Natl. Acad. Sci. USA **117**, 6409 (2020).

[23] J. Tomczak, P. Liu, A. Toschi, G. Kresse, and K. Held, Eur. Phys. J.: Spec. Top. **226**, 2565 (2017).

[24] D. Pashov, S. Acharya, W. R. Lambrecht, J. Jackson, K. D. Belashchenko, A. Chantis, F. Jamet, and M. van Schilfgaarde, Comput. Phys. Commun. **249**, 107065 (2020).

[25] T. Kotani, M. van Schilfgaarde, and S. V. Faleev, Phys. Rev. B **76**, 165106 (2007).

[26] H. Park, Ph.D. thesis, Rutgers University School of Graduate Studies, New Brunswick, NJ, 2011.

[27] Z. Yin, K. Haule, and G. Kotliar, Nat. Phys. **10**, 845 (2014).

[28] K. Haule, Phys. Rev. B **75**, 155113 (2007).

[29] P. Werner, A. Comanac, L. de' Medici, M. Troyer, and A. J. Millis, Phys. Rev. Lett. **97**, 076405 (2006).

[30] K. Haule, C.-H. Yee, and K. Kim, Phys. Rev. B **81**, 195107 (2010).

[31] T. Miyake, F. Aryasetiawan, and M. Imada, Phys. Rev. B **80**, 155134 (2009).

[32] E. Şaşıoğlu, C. Friedrich, and S. Blügel, Phys. Rev. B **83**, 121101(R) (2011).

[33] S. Acharya, D. Pashov, F. Jamet, and M. van Schilfgaarde, Symmetry **13**, 169 (2021).

[34] W.-M. Huang and H.-H. Lin, Sci. Rep. **9**, 5547 (2019).

[35] L. C. Rhodes, M. D. Watson, A. A. Haghighirad, D. V. Evtushinsky, and T. K. Kim, Phys. Rev. B **101**, 235128 (2020).

[36] S. Acharya, D. Pashov, F. Jamet, and M. van Schilfgaarde, Phys. Rev. Lett. **124**, 237001 (2020).

[37] S. Acharya, D. Pashov, E. Chachkarova, M. Van Schilfgaarde, and C. Weber, Appl. Sci. **11**, 508 (2021).

[38] B. Zeng, G. Mu, H. Luo, T. Xiang, I. Mazin, H. Yang, L. Shan, C. Ren, P. Dai, and H.-H. Wen, Nat. Commun. **1**, 112 (2010).

[39] J. Bardeen, L. N. Cooper, and J. R. Schrieffer, Phys. Rev. **108**, 1175 (1957).

[40] S. N. Bose, Z. Phys. **26**, 178 (1924).

[41] S. N. Bose, Z. Phys. **27**, 384 (1924).

[42] A. Einstein, Sitzungsber. Preuss. Akad. Wiss., Phys.-Math. Kl. **1924**, 261 (1924).

[43] Y. Uemura, Physica C (Amsterdam) **185**, 733 (1991).

[44] K. Matsuura, Y. Mizukami, Y. Arai, Y. Sugimura, N. Maejima, A. Machida, T. Watanuki, T. Fukuda, T. Yajima, Z. Hiroi, K. Y. Yip, Y. C. Chan, Q. Niu, S. Hosoi, K. Ishida, K. Mukasa, S. Kasahara, J.-G. Cheng, S. K. Goh, Y. Matsuda *et al.*, Nat. Commun. **8**, 1143 (2017).

[45] S. Hosoi, K. Matsuura, K. Ishida, H. Wang, Y. Mizukami, T. Watashige, S. Kasahara, Y. Matsuda, and T. Shibauchi, Proc. Natl. Acad. Sci. USA **113**, 8139 (2016).

[46] P. Reiss, D. Graf, A. A. Haghighirad, W. Knafo, L. Drigo, M. Bristow, A. J. Schofield, and A. I. Coldea, Nat. Phys. **16**, 89 (2020).

[47] https://www.hpc.cam.ac.uk.